# The in-flight spectroscopic performance of the Swift XRT CCD camera during 2006-2007

O. Godet[a], A. P. Beardmore[a], A. F. Abbey[a], J. P. Osborne[a], K. L. Page[a], L. Tyler[a], D. N. Burrows[c], P. Evans[a], R. Starling[a], A. A. Wells[a], L. Angelini[b], S. Campana[d], G. Chincarini[d,e], O. Citterio[d], G. Cusumano[f], P. Giommi[g], J. E. Hill[b], J. Kennea[c], V. LaParola[f], V. Mangano[f], T. Mineo[f], A. Moretti[d], J. A. Nousek[c], C. Pagani[c], M. Perri[g], M. Capalbi[g], P. Romano[d,e], G. Tagliaferri[d], F. Tamburelli[g]

[a]University of Leicester, University Road, Leicester, LE1 7RH, UK;
[b]NASA-GSFC, Greenbelt, MD 20771, USA;
[c]Pennsylvania State University, 525 Davey Lab, University Park, PA 16802, USA;
[d]INAF-Osservatorio Astronomico di Brera, Via E. Bianchi 46, 23807, Merate, LC, Italy;
[e] Università degli Studi di Milano, Bicocca, Piazza delle Scienze 3, I-20126, Milano, Italy;
[f]INAF-IASF, Via U. La Malfa 153, 90146 Palermo, Italy;
[g]ASI-ASDC, Via G. Galilei, I-00044 Frascati, Italy

## ABSTRACT

The Swift X-ray Telescope focal plane camera is a front-illuminated MOS CCD, providing a spectral response kernel of 135 eV FWHM at 5.9 keV as measured before launch. We describe the CCD calibration program based on celestial and on-board calibration sources, relevant in-flight experiences, and developments in the CCD response model. We illustrate how the revised response model describes the calibration sources well. Comparison of observed spectra with models folded through the instrument response produces negative residuals around and below the Oxygen edge. We discuss several possible causes for such residuals. Traps created by proton damage on the CCD increase the charge transfer inefficiency (CTI) over time. We describe the evolution of the CTI since the launch and its effect on the CCD spectral resolution and the gain.

**Keywords:** CCD, X-rays, spectroscopy, Charge Transfer Inefficiency

## 1. INTRODUCTION

The Swift gamma-ray burst satellite[1] was successfully launched on 2004 November 20. Since then, it has provided observations and positions of GRBs and their afterglows to observers and robotic telescopes typically within a minute, thanks to its three instruments: the wide-field Burst Alert Telescope[2] and the two narrow-field instruments, X-Ray Telescope[3] and UV/Optical Telescope[4]. When a GRB is detected by the BAT and a slew is possible, Swift automatically re-points to bring the burst within the field of view of the XRT and the UVOT.

The XRT uses a grazing incidence Wolter-1 telescope consisting of a thermally controlled carbon fibre telescope tube, an X-ray mirror system of 12 concentric gold-coated electroformed Ni shells with a 3.5m focal length, and a Focal Plane Camera Assembly (FPCA) housing an e2v CCD-22 with $600 \times 602$ image pixels, located behind an optical blocking filter with an optical transmission of about 0.25%. The CCD is mounted on a thermoelectric cooler connected via a heat pipe to an external radiator. The FPCA also includes an autonomous Sun shutter, four $^{55}$Fe calibration sources and a substantial mass of Al proton shielding (which also reduces thermal variations). To avoid the effects of pile-up, the XRT is able to autonomously select one of the three following readout modes[5] according to the source brightness: Photo-diode (PD) mode at highest count rates with a 0.14 ms time resolution and no spatial information; Windowed Timing (WT) mode at moderate count rates with a

---

Further author information: (Send correspondence to O.G.)
O.G.: E-mail: og19@star.le.ac.uk, Telephone: +44 116 223 1039
A.P.B.: E-mail: apb@star.le.ac.uk, Telephone: +44 116 252 3583

1.8 ms time resolution and 1-D spatial information; at lower count rates Photon Counting mode (PC) with a 2.5 s time resolution and 2-D spatial information.

During the first year in orbit two major incidents occurred which required modification of the instrument's operation, although they have not affected its scientific productivity. First, before the CCD was cooled to its nominal operating temperature of $-100°$C, the XRT thermo-cooler (TEC) power supply system apparently failed, and therefore the XRT has to rely on passive cooling via the heat pipe and radiator in combination with enhanced management of the spacecraft orientation to reduce the radiator view of the sunlit earth. In flight the XRT is nowadays operated with CCD temperatures of -75 to -52°C (see Kennea et al.[6] for more details). Secondly, on 2005 May 27 the XRT was hit by a particle (micro-meteoroid) which scattered off the mirror system to hit several CCD pixels, causing new bright pixels, one bright column and two bright column segments[7]. Charge leakage from the top of the bright column affects its immediate neighbours. The evolution of charge leakage depends on the CCD temperature which can now only be controlled by orientation of the spacecraft. After this event, the optical filter showed no sign of damage. Similar events were also observed in the XMM-Newton EPIC MOS CCDs. The bright pixels and columns have been vetoed on-board for the PC and WT modes. This is impossible in PD mode so that mode is no longer used, which had the beneficial effect of reducing the CCD temperature.

These two incidents had no direct impact on the spectroscopic performance of the XRT, or its ability to image and locate new GRBs. Indeed, the XRT routinely measures the early X-ray light-curves and spectra of all the GRB afterglows at which it is promptly pointed (hence 95% of the 183 GRBs detected by the BAT for which a spacecraft slew was possible within 5 minutes after the BAT trigger were detected by the XRT up until the middle of July 2007; the BAT has detected a total of 243 GRBs up until the middle of July 2007). These observations have revealed previously unexpected multiple breaks[8,9] and flares in the early X-ray light-curves[8,10–13] suggesting extended activity of the central engine up to $10^5$ s after the trigger for long and short GRBs; which challenges the current progenitor models. Essential spectral and temporal information was also obtained with the XRT for the peculiar event GRB 060218 showing for the first time the rise of a supernova[14]. The XRT has also discovered the first short burst afterglow[15] and provided accurate locations of several short GRBs, which are associated with elliptical galaxies or star-forming galaxies, the burst being located in the outskirts of the galaxy in the latter case; these results tend to indicate that short GRBs are likely to be due to binary compact object spiral-in and collision[16,17]. The XRT also provides essential information for non-GRB targets, for example with the follow-up of the recurrent nova RS Ophiuchi[18] or the micro-quasar GRO J1655-40[19]. The fraction of time spent on non-GRB targets (excluding the calibration targets) is $\sim 39.4\%$ since the launch, and this is expected to increase over time.

In this paper, we concentrate on the XRT CCD in-flight spectral calibration, and describe recent improvements to the response model made available as response matrices through the HEASARC caldb (RMF version 009[20]). The results obtained during the pre-flight calibration were covered in Osborne et al.[21].

## 2. IN-FLIGHT CALIBRATIONS

Since the FPCA front door was opened, spectroscopic calibrations have been only performed using a set of well known celestial objects observed every six months in order to monitor the change in the spectral response (see Table 1). The fraction of time spent on calibration targets is $\sim 7.5\%$ since the launch. Many of our calibration targets are also used by other X-ray observatories. This allows us to perform cross-calibration campaigns with different X-ray instruments (e.g. the XMM-Newton EPIC MOS cameras for the quasar 3C 273 and the blazar Mkn 421). In addition, we make use of four $^{55}$Fe calibration sources permanently illuminating the non-imaging area of the CCD. In order to optimise and facilitate the scheduling of the calibration targets, a new state was implemented on-board the XRT in 2007 May. This new state allows us, for instance, to control the observation mode while the XRT is still in auto-state depending on the purpose of the observations.

## 3. RESPONSE MODEL DEVELOPMENTS FROM JANUARY 2006 TO JUNE 2007

When an X-ray photon interacts within the CCD, it generates a charge cloud which is collected in the depletion region after spreading in the bulk of the detector. The charge cloud may spread into more than one pixel depending on its energy and location of interaction. To compute the response matrices we stack simulated

Table 1. Summary of the in-flight calibration targets used up to July 2007.

| Object | Type | Mode | Purpose | Exposure (ks) |
|--------|------|------|---------|---------------|
| RXJ 1856.5-3754 | Neutron star | PC/WT | Low energy response | 55/47 |
| PKS 0745-19 | Cluster of galaxies | PC | Effective area | 61 |
| 2E 0102-7217 | SNR | PC<br>WT | Gain, energy resolution and shoulder | 76<br>55 |
| Cas A | SNR | PC<br>WT | Energy scale offset, gain, shoulder, CTI and energy resolution | 144<br>51 |
| 3C 273 | Quasar | WT | Effective area and cross-calibration with XMM-Newton | 18 |
| PSR 0540-69 | Pulsar | PC/WT | Effective area | 56/26 |
| PKS 2155-304 | Blazar | WT | Effective area (cross-calibration with XMM-Newton) | 13 |
| NGC 7172 | Seyfert 2 | PC | Redistribution | 15 |
| G21.5 | SNR | PC | High-energy shelf | 40 |
| Mkn 421 | Blazar | WT | Effective area and cross-calibration with XMM-Newton | 33 |
| Crab | Pulsar | WT | Effective area | 46 |

spectra of monochromatic X-rays. We use the grade recognition process used in the analysis software (for PC mode this is a $3 \times 3$ pixel matrix centred on the highest pixel). To avoid noise being included in the charge summation and excessive telemetry usage, a threshold is set on-board below which pixels are not considered.

The X-ray spectrum resulting from monochromatic radiation significantly differs from a simple Gaussian, it consists of six components: a Gaussian peak with a shoulder on the low energy side of the peak, an escape peak and a Si K$\alpha$ fluorescence peak if the photon energy is above the Si K-shell edge, a shelf extending to low energies, and at the very lowest energies a noise peak (of which only the high energy side may be seen above threshold).

Below 1.5 keV, the shoulder and shelf are mainly produced by the charge losses at the interface between the SiO$_2$ layer and the active silicon volume of the open electrode, possibly due to a local inversion of the electric field near the detector surface. Above 1.5 keV, the shoulder and the shelf are produced by several processes: (i) sub-threshold losses; (ii) recombination and trapping in the bulk of the detector; (iii) inhomogeneity of the electric field in the depletion depth, in addition to the surface losses. Their exact shapes depend on the readout mode, and hence they are different for the PC and WT modes. Both above and below 1.5 keV, the main peak broadens with time due to the degradation of the charge transfer efficiency, producing a larger shoulder at lower energies (see Section 5).

Changes in our spectral response code have been made in order to better reproduce the different components mentioned above. The recent improvements described below have been released as new spectral response files (version v009[20]).

## 3.1 The shelf from photons above $\sim 2$ keV

The new response matrice files (v009 RMFs) include an empirical rescaling of the low energy shelf made by X-rays above 2 keV, which significantly improve the quality of spectral fits to the calibration sources (see Fig. 1). This was previously incompletely modelled for either PC or WT modes, resulting in an underestimation of the modelled redistributed counts when fitting spectra of heavily absorbed sources (e.g. $N_H \geq 10^{22}$ cm$^{-2}$).

## 3.2 The shoulder from photons above $\sim 1.5$ keV

Before the v009 release of the calibration files, the shoulder, which was modelled by artificially increasing the event split threshold in order to increase the sub-threshold losses, was not reproduced well (see Fig. 6a in Osborne et al.[21]). We showed that modification of the shape of the charge cloud formed in the field-free region using the
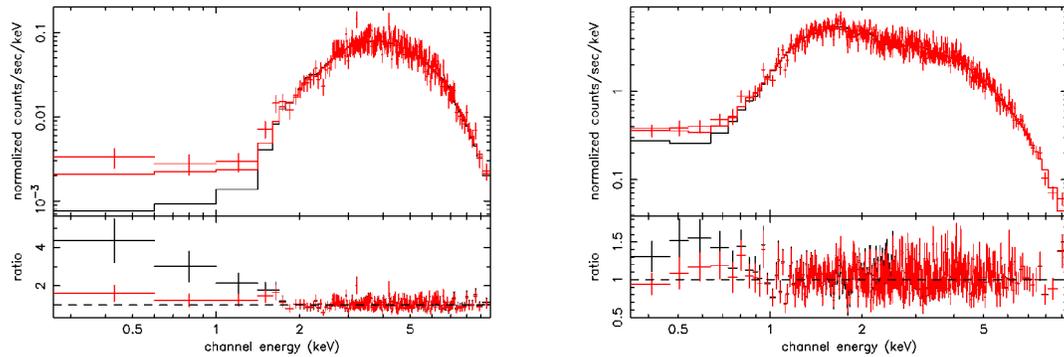
Figure 1. Left: XRT PC grade 0-12 spectrum of NGC 7172 using the new v009 (red) and previous v008 (black) response files. The use of a WABS*POWERLAW model gives a value of $N_H \sim 7.3 \times 10^{22}$ cm$^{-2}$. Right: XRT WT grade 0-2 spectrum of the X-ray binary 4U 1608 using the new v009 (red) and previous v008 (black) response files. The use of a WABS*(POWERLAW+DISKBB) model gives a value of $N_H \sim 10^{22}$ cm$^{-2}$.

formalism described in Pavlov & Nousek[22] can lead to a more physical modelling of the shoulder (see Fig. 6b in Osborne et al.[21]), the shape being no longer a 2-D Gaussian (although a 2-D Gaussian remains sufficient in the depletion region). Fig. 2 shows the relatively good agreement of the model with the very complicated spectrum of the SNR Cas A (the North knot as noted in Fig. 2).
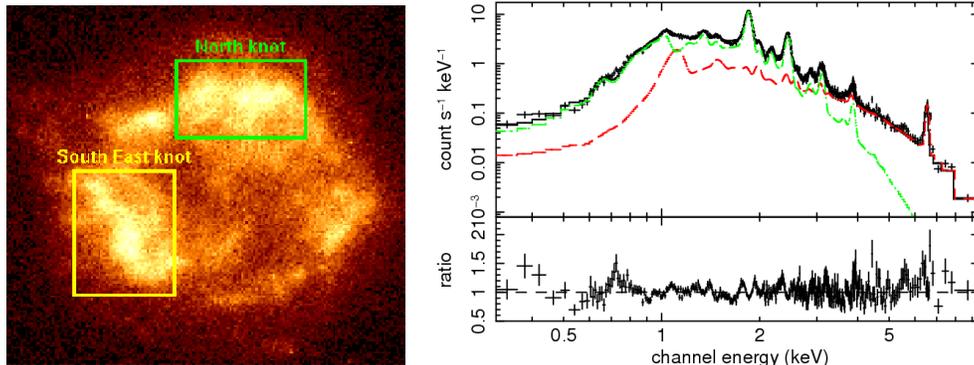


Figure 2. Left: PC grade 0 image of the SNR Cas A. Right: PC grade 0 spectrum of the North knot of the SNR Cas A (see the image on the left). The data were taken in 2005 February 17. The spectrum is fit using a PHABS(VNEI+VNEI) model (see Willingale et al.[24]).

## 4. THE RESIDUALS AROUND AND BELOW THE OXYGEN EDGE

The fits of several continuum sources reveal negative (less than 20%) residuals around the Oxygen edge (0.54 eV) using v008 and v009 RMFs.

Recently, observational evidence has shown that the CCD bias level can significantly vary during the timescale of an orbital snapshot on an astrophysical target. The bias level is mode-dependent and is subtracted on-board during the XRT observations. Bias variations during a snap-shot can occur due to changes in the CCD temperature and/or scattered optical light from the sunlit Earth[23]. This can result in energy scale offsets, which give rise to residuals when fitting spectra, especially at low energies (e.g. around the Oxygen edge). Energy scale offsets can be seen in both PC and WT modes. A new command option was implemented in the 2.6 XRT software (WTBIASDIFF) in order to correct the WT data for this effect. A tool XRTPCBIAS included in the 2.7

XRT software* has been released in July 2007 by the XRT software team, which corrects the PC data. The use of these contemporary time-dependent bias estimators can significantly improve the energies of low energy events (see Fig. 3).

Charge transfer inefficiency due to accumulating proton damage also results in a slow change in the energy scale. This is discussed in Section 5.
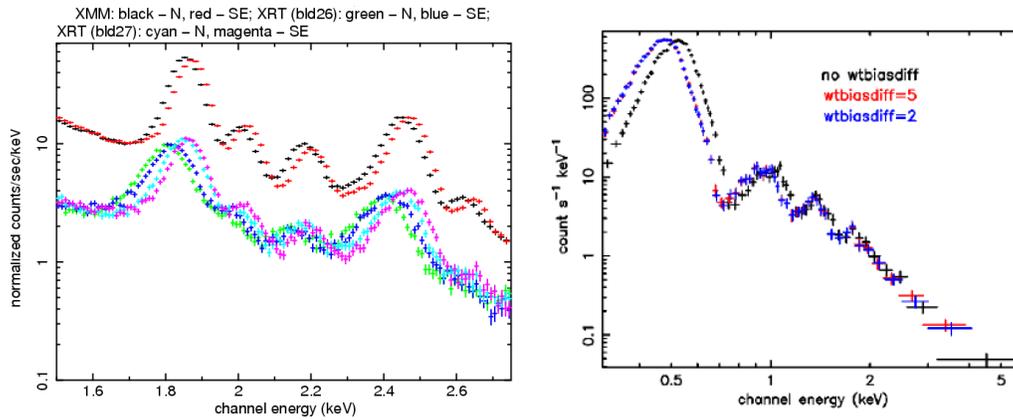


Figure 3. Left: Comparison of the energy centroid of the Si and S lines in the North (N) and South East (SE) knots of the SNR Cas A as observed by the XMM MOS cameras (N: black; SE: red) and the XRT (N: green, cyan; SE: blue, magenta). The green and blue crosses correspond to XRT/PC grade 0 data for which the bias was contaminated by optical light from the sunlit Earth. The data were processed with the CALDB2.6 software which does not allow to bias corrections. In this case, an energy scale offset is observed when compared with the XMM MOS curves. The cyan and magenta crosses correspond to the same data processed with the new CALDB2.7 software including the tool XRTPCBIAS, which corrects the data. Right: XRT WT grade 0-2 spectrum of RS Ophiuchi: (*black*) the data not corrected to the bias problem and (*red and blue*) the data corrected using the new command option WTBIASDIFF.

Cross-calibration performed with other X-ray instruments in orbit such as *XMM-Newton* and *Suzaku* on the supernova remnant 2E 0102-7217 reveals that at least these CCD cameras seem to suffer from an overestimation of the model with respect to the data around the Oxygen edge. Recently, the MOS calibration team has decided to apply an *ad hoc* correction to their quantum efficiency (QE) by decreasing the QE below the Oxygen edge by 10-15%, in order to correct the residuals. We are investigating whether a similar approach could work in the case of the XRT, once the effects of energy scale offset have been corrected.

## 5. CHARGE TRANSFER INEFFICIENCY

CCD detectors provide good X-ray imaging and spectroscopic performance. However, the CCD energy resolution and gain degrade with time due to the increase of the CTI. The main origin of CTI is the increase of charge traps, which are mainly due to the irradiation of high-energy protons on the CCD passing through the shielding. Although the low-Earth orbit of *Swift* and the thick Al shielding around the CCD detector reduce the proton flux, the frequent passages of the spacecraft through the South Atlantic Anomaly (SAA) can cause formation of charge traps, and hence an increase of CTI. Since the launch, the FWHM measured using the four $^{55}$Fe calibration sources (located in each corner of the CCD; the area of the detector covered by these corner sources being small and outside the imaging area) increased from 146 eV at 5.9 keV in Feb 2005 to 210 eV in March 2007 when using the *bad and good columns* (i.e. columns with and without significant traps), respectively. The broadening of the line is due to the energy scale shifting effect of traps in the pixels through which the charge has to be transported. The increase of traps in the CCD imaging area, the serial register and the frame-store area also causes energy scale offset as shown in the left panel in Fig. 4. In this Figure, the data were processed with a gain file not corrected from the CTI increase.

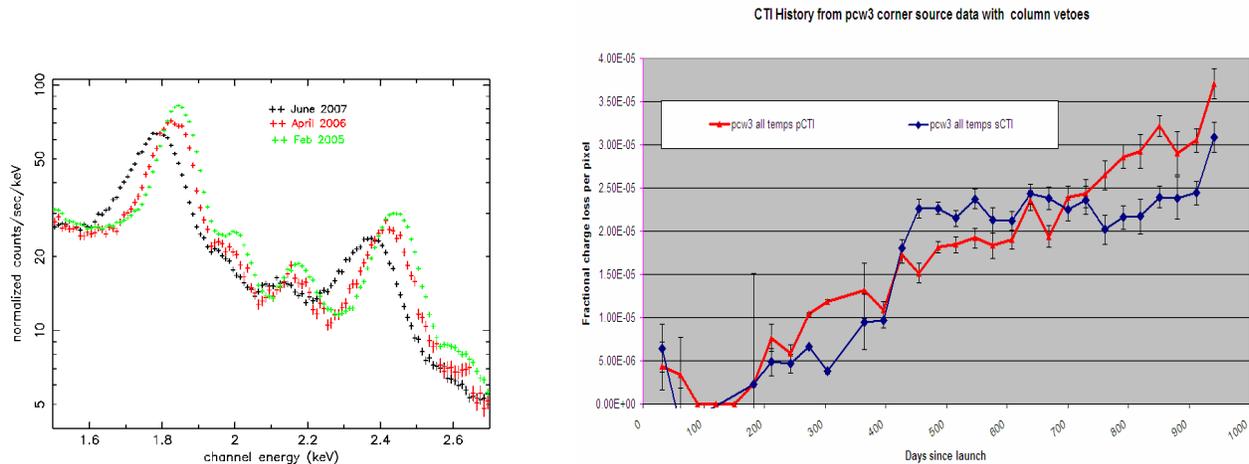*see the following URL: http://heasarc.gsfc.nasa.gov/docs/software/lheasoft/release_ notes.html

Figure 4. Left: WT grade 0-2 spectrum of the SNR Cas A in the energy band of the Si and S lines at different epochs since the launch showing the degradation of the energy resolution and the gain due to the increase of traps in the CCD. The WT data were processed with the command option WTBIASDIFF correcting the bias level if corrupted (see Section 4). The measurements of the energy centroid of the Si and S lines imply an energy shift of about -50 eV from February 2005 to June 2007, when the increase of CTI over time is not taking into account in the gain file. The FWHM of the Si line increases from 105 eV in February 2005 to about 131 eV in June 2007. Right: Evolution of the serial (blue) and parallel (red) CTI with time since the launch as measured using the four corner source data. The CTI values were computed vetoing the columns with significant traps.

Since we do not have any on-board calibration source illuminating the imaging area, we use four $^{55}$Fe (5.9 keV) calibration sources to track the temporal evolution of CTI. We define a parallel and serial CTI as follows:

$$\text{CTI}_{p,s} = \frac{E_i - E_{p,s}}{n \times E_i}$$

where $\text{CTI}_{p,s}$ corresponds to the parallel and serial CTI respectively, and $E_i$ is the measured energy centroid of the corner source CS3 closest to the output amplifier (bottom left of the imaging area), which does not suffer from the CTI loss in the imaging area. $E_{p,s}$ is the measured energy centroid of the source located in the top left and bottom right corner of the imaging area, respectively. $n$ is the number of pixels that the charge has to pass through in being readout (i.e. transfered down the CCD and then along the readout strip). Note that we used only the columns with no significant traps to do the computation, hence the CTI values derived are free from the effects of the traps. The computed parallel and serial CTI values (see the right panel Fig. 4) as well as the gain values of the corner source CS3 closest to the output amplifier are used to generate an epoch-dependent gain file. The gain variations measured from the corner source CS3 are due to the CTI increase over time in the store-frame area (in which no CTI measurements can be performed since no calibration sources illuminate this part of the CCD) and/or possible gain variations of the output FET (Field Effect Transistor) with time. Up until July 2007, the gain of the corner source CS3 increased by about 1%. While the parallel CTI increased relatively steadily since the launch from $5 \times 10^{-6}$ to $3.5 \times 10^{-5}$ in June 2007 (see Fig. 4), the serial CTI increased rapidly in a short period of time around November 2005 and stayed relatively constant around $2.5 \times 10^{-5}$ from December 2005 up to March 2007.

In order to correct the data from the effects of traps, we plan to determine the location and depth of the largest traps and implement a correction in the data processing software. We need to use a stable, sufficiently extended and emission line-dominated source to map the central imaging area (a $200 \times 600$ pixel window in PC mode and a 200 pixel window in WT). Supernova remnants (SNRs) are the best astrophysical sources. We plan to use the SNR Cas A which has intense Silicon and Sulphur lines. Although the energy centroids show an energy variation of less than $\pm 10$ eV (at the energy of the Si and S lines) across the remnant[24], the energy variation due to traps that we want to measure are much larger. The only drawback of this method is that we cannot map all the imaging area ($600 \times 602$ pixels) due to the excessive exposure time that would be needed.

A more efficient and simpler approach would be to use the charge injection technique[25] to measure the CTI for each column, as it has been done for the Soft X-ray cameras on-board *Suzaku*[26], since we can then correct all the CCD imaging area without long calibration exposures. We are undertaking further work to verify the feasibility of this technique in the case of the e2v CCD-22 used in the XRT.

## 6. REDUCTION OF NOISE BY SUBSTRATE VOLTAGE CHANGE

The loss of the active cooling causes the XRT to operate at higher than expected temperatures (see Section 1); this generates significant thermally-induced noise appearing as low energy events. Raising the substrate voltage as described in Osborne et al.[21] will allow a reduction of this noise and the use of lower energy X-ray events, since the volume of Silicon in which carriers are generated is reduced.

Osborne et al.[21] have shown that raising the substrate voltage will cause a decrease of the depletion depth, resulting in a migration of events to higher grades (hence, an increase of the sub-threshold losses) and a slight decrease of the QE. We performed observations of Cas A (2.2 ks in PC and 0.8 ks in WT) and the Crab (0.6 ks in WT) with raised substrate voltage ($V_{ss}$ = 6 V instead of 0 V). Fig. 5 shows that the changes in the effective area are small between $V_{ss}$ = 6 V and 0 V (i.e. less than 15% at 6 keV). The gain will also change when the substrate voltage settings are modified, because the gain of the output FET, which works in a source follower configuration, will slightly change in this new configuration.
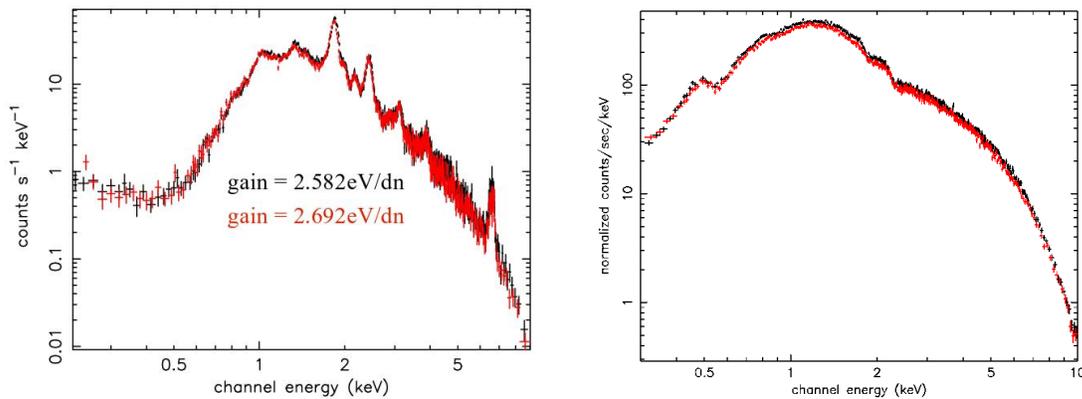


Figure 5. Left: WT grade 0-2 spectra of Cas A with the substrate voltage $V_{ss}$ = 6 V (red crosses) and $V_{ss}$ = 0 V (black crosses). Note that the gain changed between the two configurations, since the gain of the output FET slightly changed between the two configurations (see text). Right: WT grade 0-2 off-pulse spectra of the Crab with $V_{ss}$ = 6 V (red crosses) and $V_{ss}$ = 0 V (black crosses). The two plots show that the changes in the effective area, hence the QE, are minimal between the two configurations.

## 7. CONCLUSION

We showed that our Monte-Carlo code computing the PC and WT RMFs allows us to describe the CCD response well. Thus, the v009 RMF files release in July 2007 allow a better modelling of the low-energy shelf of heavily absorbed sources and a better physical description of the origin of the shoulder from photons above 1.5 keV. We also showed that energy scale offsets due to corruption of the bias level in both PC and WT modes can limit the improvements of the instrument spectral response, especially at low energies. New tool xrtpcbias and the new command option wtbiasdiff have been provided by the XRT software team to correct the bias level in both PC and WT mode, and hence suppress energy scale offset. These tools are included in the 2.7 XRT software package recently released.

We are working on a more complete trap characterisation. To do so, the XRT began observing the SNR Cas A for 80 ks in PC mode and 50 ks for WT. Because of the development of traps with time in the CCD detector,

we also outline the importance to use an on-board calibration source which fully illuminates the focal plane, for instance as used on-board XMM-Newton, for future X-ray CCD instruments.

Finally, in order to improve further the XRT spectral performance, we plan to raise permanently the substrate voltage to $V_{ss} = 6\,V$ on-board before the end of 2007. An intense phase of re-calibration of the instrument will shortly follow to update the spectral response files, the gain file and the ground data processing software.

## 7.1 Acknowledgements

## REFERENCES

[1] N. Gehrels et al., "The Swift Gamma-Ray Burst Mission", *ApJ*, 611, 1005, 2004

[2] S. Barthelmy et al., "The Burst Alert Telescope (BAT) on the Swift MIDEX Mission", *Space Science Reviews*, 120, 143, 2005

[3] D. N. Burrows et al., "The Swift X-Ray Telescope", *Space Science Reviews*, 120, 165, 2005

[4] P. W. A. Roming et al., "he Swift Ultra-Violet/Optical Telescope", *Space Science Reviews*, 120, 95, 2005

[5] J. E. Hill et al., "Readout modes and automated operation of the Swift X-ray telescope", *Proc SPIE*, 5165, 217, 2004

[6] J. Kennea et al., "Controlling the Swift CCD temperature with passive cooling", *Proc SPIE*, 5898, 341, 2005

[7] A. F. Abbey et al., "Micrometeoroid damage to CCDs in XMM-Newton and Swift and its significance for future X-rays missions", Proceeding of the X-ray Universe Conference, El Escorial Spain, 2005 (see http://xmm.vilspa.esa.es/external/xmm_science/x-ray-symposium/175772_afa_micrometeoroids.pdf)

[8] B. Zhang et al., "Physical Processes Shaping Gamma-Ray Burst X-Ray Afterglow Light Curves: Theoretical Implications from the Swift X-Ray Telescope Observations", *ApJ*, 642, 354, 2006

[9] J. A. Nousek et al., "Evidence for a Canonical Gamma-Ray Burst Afterglow Light Curve in the Swift XRT Data", *ApJ*, 642, 389, 2006

[10] D. N. Burrows et al., "X-ray Flares in Early GRB Afterglows", *Phil. Trans. A.*, 365, 1213, 2007

[11] A. King et al., "Gamma-Ray Bursts: Restarting the Engine", *ApJ*, 630, L113, 2005

[12] D. Proga & B. Zhang, "The late time evolution of gamma-ray bursts: ending hyperaccretion and producing flares", *MNRAS*, 370, L61, 2006

[13] R. Perna et al., "Flares in Long and Short Gamma-Ray Bursts: A Common Origin in a Hyperaccreting Accretion Disk", *ApJ*, 636, L29, 2006

[14] S. Campana et al., "The association of GRB 060218 with a supernova and the evolution of the shock wave", *Nature*, 442, 1008, 2006

[15] N. Gehrels et al., "A short $\gamma$-ray burst apparently associated with an elliptical galaxy at redshift z = 0.225", *Nature*, 437, 851, 2005

[16] D. Eichler et al., "Nucleosynthesis, neutrino bursts and gamma-rays from coalescing neutron stars", *Nature*, 340, 126, 1989

[17] S. Rosswog, "Fallback accretion in the aftermath of a compact binary merger ", *MNRAS*, 376, 48, 2007

[18] M. F. Bode et al., "Swift Observations of the 2006 Outburst of the Recurrent Nova RS Ophiuchi. I. Early X-ray Emission from the Shocked Ejecta and Red Giant Wind", *ApJ*, 652, 629, 2006

[19] C. Brocksopp et al., "The 2005 outburst of GRO J1655-40: spectral evolution of the rise, as observed by Swift", *MNRAS*, 365, 1203, 2006

[20] Campana et al., "Swift CALDB Release Note Swift-XRT-CALDB-09: Response matrices and Ancillary Response Files", 2007 (see http://swift.gsfc.nasa.gov/docs/heasarc/caldb/swift/docs/xrt/SWIFT-XRT-CALDB-09_v2.pdf)

[21] J. Osborne et al., "The in-flight spectroscopic performance of the Swift XRT CCD camera", *Proc SPIE*, 5898, 352, 2005

[22] G. G. Pavlov & J. A. Nousek, "Charge diffusion in CCD X-ray detectors", *NIMA*, 439, 348, 1999

[23] A. P. Beardmore et al., "Describes the effects contributing to the energy scale offset (spectral analysis)", 2007 (see http://swift.gsfc.nasa.gov/docs/heasarc/caldb/swift/docs/xrt/xrt_bias.pdf)

[24] R. Willingale et al., "X-ray spectral imaging and Doppler mapping of Cassiopeia A", *A&A*, 381, 1039, 2002

[25] G. Y. Prigozhin et al., "X-ray CCD with charge-injection structure", *Proc. SPIE*, 5501, 357, 2004

[26] H. Nakajima et al., "Performance of the Charge Injection Capability of Suzaku XIS", *PASJ*, arXiv:0705.1771, 2007